A&A 636, A55 (2020)
https://doi.org/10.1051/0004-6361/201936765

Astronomy & Astrophysics

Rise and fall of the high-energy afterglow emission of GRB 180720B

M. Ronchi[1], F. Fumagalli[1], M. E. Ravasio[1], G. Oganesyan[2,3,4], M. Toffano[5,6], O. S. Salafia[6,7], L. Nava[6,8,9], S. Ascenzi[6], G. Ghirlanda[6,7], and G. Ghisellini[6]

[1] Universitá degli Studi di Milano-Bicocca, Dip. di Fisica "G. Occhialini", Piazza della Scienza 3, 20126 Milano, Italy
e-mail: m.ronchi26@campus.unimib.it
[2] Gran Sasso Science Institute, Viale F. Crispi 7, 67100 L'Aquila, Italy
[3] INFN – Laboratori Nazionali del Gran Sasso, 67100 L'Aquila, Italy
[4] INAF – Osservatorio Astronomico d'Abruzzo, Via M. Maggini SNC, 64100 Teramo, Italy
[5] Universitá degli Studi dell'Insubria, Via Valleggio 11, 22100 Como, Italy
[6] INAF – Osservatorio Astronomico di Brera, Via E. Bianchi 46, 23807 Merate, Italy
[7] INFN – Sezione di Milano-Bicocca, Piazza della Scienza 3, 20126 Milano, Italy
[8] INFN – Sezione di Trieste, Via Valerio 2, 34149 Trieste, Italy
[9] Institute for Fundamental Physics of the Universe (IFPU), 34151 Trieste, Italy

Received 23 September 2019 / Accepted 7 March 2020

ABSTRACT

The gamma-ray burst (GRB) 180720B is one of the brightest events detected by the *Fermi* satellite and the first GRB detected by the H.E.S.S. telescope above 100 GeV, at around ten hours after the trigger time. We analysed the *Fermi* (GBM and LAT) and *Swift* (XRT and BAT) data and describe the evolution of the burst spectral energy distribution in the 0.5 keV–10 GeV energy range over the first 500 s of emission. We reveal a smooth transition from the prompt phase, dominated by synchrotron emission in a moderately fast cooling regime, to the afterglow phase whose emission has been observed from the radio to the gigaelectronvolts energy range. The LAT (0.1–100 GeV) light curve initially rises ($F_{\rm LAT} \propto t^{2.4}$), peaks at ∼78 s, and falls steeply ($F_{\rm LAT} \propto t^{-2.2}$) afterwards. The peak, which we interpret as the onset of the fireball deceleration, allows us to estimate the bulk Lorentz factor $\Gamma_0 \sim 150$ (300) under the assumption of a circum-burst medium with a wind-like (homogeneous) density profile. We derive a flux upper limit in the LAT energy range at the time of H.E.S.S. detection, but this does not allow us to unveil the nature of the high-energy component observed by H.E.S.S. We fit the prompt spectrum with a physical model of synchrotron emission from a non-thermal population of electrons. The 0–35 s spectrum after its $EF(E)$ peak (at 1–2 MeV) is a steep power law extending to hundreds of megaelectronvolts. We derive a steep slope of the injected electron energy distribution $N(\gamma) \propto \gamma^{-5}$. Our fit parameters point towards a very low magnetic field ($B' \sim 1$ G) in the emission region.

Key words. γ-ray burst: general – radiation mechanisms: non-thermal – relativistic processes – acceleration of particles

1. Introduction

Despite having been discovered more than 50 years ago, from a theoretical point of view gamma-ray bursts (GRBs) still represent one of the most challenging transient sources of high-energy photons in the Universe. Even if some of the observational features can be explained within the context of the standard fireball model developed by Rees & Meszaros (1992, 1994) and Meszaros & Rees (1993), there are still many important missing pieces of the GRB complex puzzle (see Meszaros 2019; Zhang 2019; Kumar & Zhang 2015; Piran 1999, 2004). The physical origin of the prompt emission, for example, is still under debate. Although the synchrotron process has been proposed as the emission mechanism responsible for the observed radiation (Rees & Meszaros 1994; Sari & Piran 1997; Kobayashi et al. 1997; Daigne & Mochkovitch 1998), for a long time the predictions of the spectral shape from a population of accelerated electrons cooling via the synchrotron process have been thought to be inconsistent with the shape of the typical observed GRB prompt emission spectra (Preece et al. 1998; Ghisellini et al. 2000; Kaneko et al. 2006; Ghirlanda et al. 2009; Nava et al. 2011; Gruber et al. 2014). For many years, this inconsistency has been the major argument against the synchrotron interpretation of the GRB prompt emission spectra. Only recently, new observational evidences were found in support of the synchrotron interpretation (Oganesyan et al. 2017, 2018, 2019; Ravasio et al. 2018, 2019a). Extending the investigations down to the X-ray and optical bands, a remarkable consistency of the observed GRB prompt spectra and synchrotron predictions has been discovered when electron cooling is taken into account. Burgess et al. (2020) also show that most of the time-resolved spectra of single-pulse *Fermi* GRBs can be successfully fitted by the synchrotron model.

The extension of the energy range towards higher energies (>100 MeV) played a fundamental role in the understanding of the nature of the high-energy component produced by these powerful transient sources. The Large Area Telescope (LAT; Atwood et al. 2009) on board the *Fermi* satellite detected and characterised the high-energy emission of several GRBs (Ajello et al. 2019). The long lasting high-energy (100 MeV–100 GeV) emission has been interpreted (see Nava 2018 for a review) as due to the external shock afterglow of the burst (Kumar & Barniol Duran 2009, 2010; Ghisellini et al. 2010; Beniamini et al. 2015). However, the characterisation of the transition from the prompt to the afterglow dominance is hampered by evidence of a superposition of these two emission components in the early phases of the LAT emission. Indeed there is some evidence for short

timescale variability above 100 MeV in some LAT bursts during the GBM emission (Ackermann et al. 2013; Ajello et al. 2019), which is a strong argument in favor of a component of internal origin.

GRB 190114C, the first GRB detected by the MAGIC telescopes (Mirzoyan 2019) with high significance, opened a new window on the interpretation of the high- and very-high-energy emission (VHE; above 100 GeV). The analysis of the spectrum at lower energies showed a clear example of the mixture of the prompt and the afterglow components in the same energy band. Using *Fermi* GRB monitor (GBM) + LAT and the *Neil Gehrels Swift* Observatory (hereafter *Swift*) X-Ray telescope (XRT) + Burst Alert Telescope (BAT) data, Ravasio et al. (2019b) show the rise of an additional non-thermal component in the keV–MeV energy range in the very early phases (~5 s after trigger time) of the prompt emission. This component, fitted by a power law $\mathrm{d}N/\mathrm{d}E \propto E^{\Gamma_{\rm PL}}$ with slope $\Gamma_{\rm PL} \sim -2$, was interpreted as the synchrotron emission from the afterglow of the burst. The difficulties in interpreting the VHE emission of GRB 190114C as synchrotron from relativistic electrons (Guilbert et al. 1983), led to ascribe its origin to synchrotron self-Compton (SSC; Derishev & Piran 2019; Fraija et al. 2019; Ravasio et al. 2019b; Wang et al. 2019).

Recently, GRB 180720B was claimed to be detected at VHE by the H.E.S.S. telescope (Ruiz-Velasco 2019; Abdalla et al. 2019) at around ten hours after the trigger time. This makes this burst a good candidate to study the origin of the VHE emission of GRBs. Even if this is not the main subject of this work, we briefly discuss the consistency of our results with the H.E.S.S. results (Sect. 5). GRB 180720B is also one of the brightest bursts ever detected by the *Fermi* satellite, with a fluence $f = 2.99 \times 10^{-4}$ erg cm^{-2} in the energy range 10–1000 keV (Roberts & Meegan 2018). Its keV–MeV prompt emission spectrum was analysed, together with another nine long bright GRBs, in Ravasio et al. (2019a) who showed the consistency of the spectral shape with synchrotron emission. It has also been detected by LAT and reported in the LAT GRB catalogue of Ajello et al. (2019). Therefore, GRB 180720B is another interesting event for studying its spectral energy distribution (SED) extending from kiloelectronvolts to gigaelectronvolts energies and possibly unveiling the transition from the prompt to the afterglow dominance and constraining the physical parameters of the emission process.

This paper is based on the study of the evolution of the spectrum of GRB 180720B during the first 500 s after trigger time, from the analysis of the data of *Fermi* (LAT+GBM) and *Swift* (BAT+XRT) satellite. In particular, we extract the light curves and analyse the spectra in order to study the temporal evolution of the SED and the consistency with the synchrotron emission, shown in Sect. 3. Interpreting the peak of the LAT light curve as due to the onset of the deceleration of the jet, we derive an estimate of the bulk Lorentz factor Γ_0 in the cases of a uniform density profile and a stellar wind density profile for the circumburst medium (Sect. 4). We discuss the theoretical implications of our results and summarise the conclusions in Sects. 5 and 6.

2. Data reduction and analysis

On 20 July 2018 at 14:21:39 UT, *Fermi*/GBM detected GRB 180720B (Roberts & Meegan 2018), which was also detected by *Swift*/BAT (Siegel et al. 2018) and *Fermi*/LAT (Bissaldi & Racusin 2018). The observed burst duration T_{90} is 49 s in the energy range 50–300 keV (Roberts & Meegan 2018). The burst was also detected by Konus-Wind (Frederiks et al. 2018), by the CALET GRB monitor (Cherry et al. 2018) and in the X-ray band by MAXI/GSC (Negoro et al. 2018) and by NuSTAR (Bellm & Cenko 2018). GRB 180720B was observed by an intensive follow-up campaign. *Swift*/XRT began observing the source 86.5 s after the BAT trigger. Sasada et al. (2018) detected a bright optical counterpart, 73 s after the trigger using the 1.5 m Kanata telescope. They measured an *R*-band apparent magnitude of $m \sim 9.4$, which corresponds to an optical flux $EF(E) \sim 1.4\,\mathrm{keV\,cm^{-2}\,s^{-1}}$ at a central frequency of about 4×10^{14} Hz. Several other optical ground telescopes observed this burst (Reva et al. 2018; Itoh et al. 2018; Kann et al. 2018; Crouzet & Malesani 2018; Horiuchi et al. 2018; Watson et al. 2018; Schmalz et al. 2018; Covino & Fugazza 2018; Lipunov et al. 2018; Jelinek et al. 2018; Zheng & Filippenko 2018; Izzo et al. 2018). The redshift was measured with the instrument X-shooter on VLT UT2 telescope (Vreeswijk et al. 2018) and has a value of $z = 0.654$. In the radio band, both the Arcminute Microkelvin Imager Large Array (AMI-LA) at 15.5 GHz (Sfaradi et al. 2018) and the Giant Metrewave radio Telescope at 1.4 GHz (Chandra et al. 2018) observed the field and detected the source.

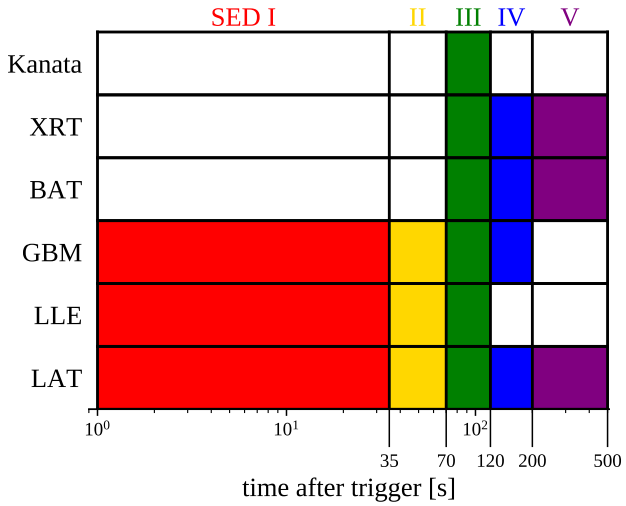

Fig. 1. Time intervals and corresponding instruments providing the spectra used for the spectral analysis of GRB 180720B. The colour code corresponding to the sequence of time intervals is used for all the following figures except for Figs. 5 and 6.

In order to study the transition from the prompt to the afterglow emission in GRB 180720B, we considered five time intervals of 0–35 s, 35–70 s, 70–120 s, 120–200 s, and 200–500 s (see Fig. 1). These time intervals were identified in red, yellow, green, blue, and purple, respectively, and this colour-code was also used in Figs. 2 and 3. The choice of these large time intervals for the spectral analysis is determined by three requirements: (1) We need sufficient signal in the energy range of the LAT low-energy (LLE) data (>30 MeV) because we are interested in studying the spectral transition from the prompt to the afterglow, which is best highlighted in the high-energy regime (i.e. above few megaelectronvolts). (2) To perform a multi-band analysis, we have to consider the different starting times of the observations in different spectral bands (i.e. the start of the *Swift*/XRT and optical observations). (3) We take into account the rise, peak, and initial decay of the *Fermi*/LAT light curve and the spectral evolution in the LAT energy range. In particular, as Fig. 2 shows, the first time interval (0–35 s) includes the main emission event of the GRB. Furthermore, up to 35 s the high-energy LAT spectrum presents different behaviour with respect to the rest of the burst (see bottom panel in Fig. 3). This aspect is discussed in Sect. 3

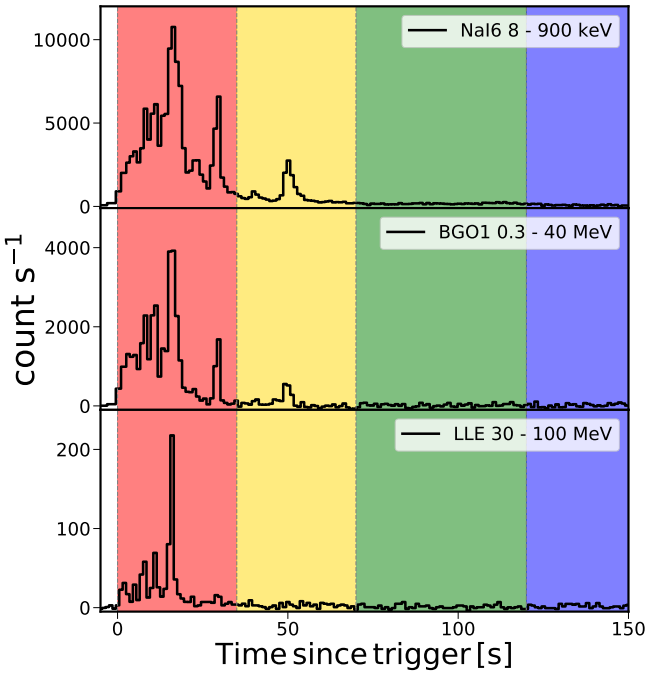

Fig. 2. Background-subtracted light curves of GRB 180720B, detected by NaI#6 (8–900 keV, *top*), BGO#1 (0.3–40 MeV, *middle*), and LAT-LLE (30–100 MeV, *bottom*). Different time intervals are highlighted with different colours, according to the colour code used in Fig. 1.

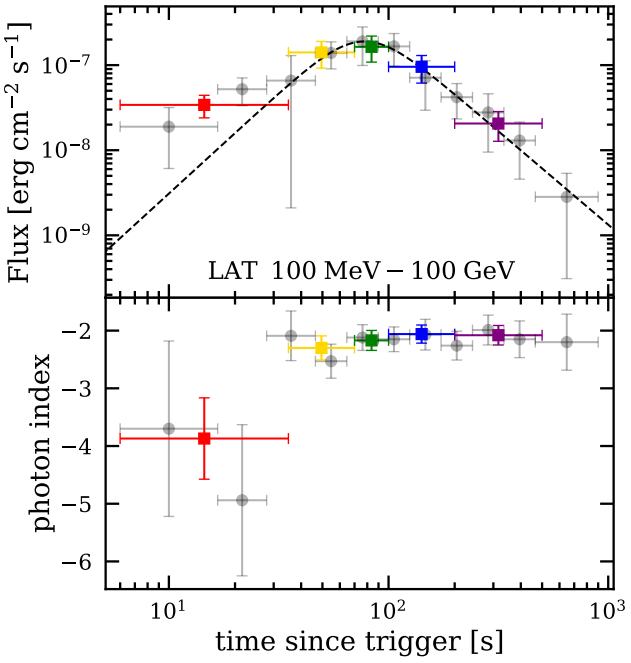

Fig. 3. *Top panel*: LAT light curve. The energy flux is integrated over the 100 MeV–100 GeV energy range. Coloured square symbols correspond to the time intervals defined in 1; grey circles show the results of the analysis with a higher time resolution. *Bottom panel*: photon indices of the power-law model used for the LAT data analysis. Same colour coding and symbols as the top panel.

in more detail. The second time interval (35–70 s) includes a second emission event visible in the GBM light curves (Fig. 2). The third time interval (70–120 s) encompasses the peak of the LAT light curve (top panel in Fig. 3) and the last two intervals (120–200 s and 200–500 s) follow its decay. In Fig. 1, for each time interval we denote the instruments we use for the analysis. In the following sections we describe the main data source and the standard procedures adopted for the data extraction.

2.1. Fermi/LAT

The LAT instrument on board *Fermi* is composed of a tracker and a calorimeter sensitive to gamma-ray photons in the energy range between 30 MeV and 300 GeV (Ackermann et al. 2013). Data extraction and analysis were performed with `gtburst`, which is distributed as part of the official `Fermitools` software[1]. The LAT data were extracted within a temporal window extending 900 s after the trigger time and filtered selecting photons with energies in the 100 MeV–100 GeV range, within a region of interest (ROI) of 12° centred on the burst position provided by *Swift*/BAT (Barthelmy et al. 2018). A further selection of photons with a zenith angle from the spacecraft axis <100° was applied to reduce the contamination of photons coming from the Earth limb. The highest photon energy is 4.9 GeV and the corresponding photon was detected by LAT 137 s after the GBM trigger. These values are consistent with those reported by the *Fermi*/LAT Collaboration (Bissaldi & Racusin 2018).

2.2. Fermi/GBM

The GBM detector on board *Fermi* is composed of 12 sodium iodide (NaI, 8 keV–1 MeV) and 2 bismuth germanate (BGO; 200 keV–40 MeV) scintillation detectors (Meegan et al. 2009). We analysed the data from the two NaI detectors and the BGO detector with the highest count rates, namely NaI#6, NaI#8 and BGO#1. For each detector, we retrieved the data and the most updated response matrix files from the *Fermi* website[1].

Spectra were extracted with `gtburst`: we selected energy channels in the range 8–900 keV for NaI detectors, and 0.3–40 MeV for the BGO detector, and excluded channels in the 30–40 keV range owing to the presence of the iodine K-edge at 33.17 keV[2]. The background was modelled over pre- and post-burst time intervals with a polynomial whose order is selected automatically by `gtburst`.

We also fitted the first two time intervals by combining the GBM with the LAT LLE data (Pelassa et al. 2010). The LAT-LLE data were retrieved from the *Fermi* LLE Catalog[3] and reduced with a similar procedure as for the GBM data through `gtburst`. The LLE spectra analysed cover the energy range 30–100 MeV (e.g. Ajello et al. 2019).

2.3. Swift

The BAT on board *Swift* (Gehrels et al. 2004) is a coded aperture mask which triggers GRBs by imaging photons in the energy range 15–350 keV. We downloaded BAT event files from the *Swift* archive[4]. The BAT spectra were extracted with the `batbinevt` task of HEASOFT package (v6.25) and corrected for systematic errors (with the `batupdatephakw` and `batphasyserr` tasks). The response matrices were computed

[1] https://fermi.gsfc.nasa.gov/ssc/data/

[2] https://fermi.gsfc.nasa.gov/ssc/data/analysis/GBM_caveats.html

[3] https://heasarc.gsfc.nasa.gov/W3Browse/fermi/fermille.html

[4] http://heasarc.gsfc.nasa.gov/cgi-bin/W3Browse/swift.pl

by the batdrmgen tool for the time intervals before, during, and after the *Swift* slew.

The XRT focusses photons in the 0.3–10 keV energy range (Wells et al. 2004). We downloaded the XRT event files from *Swift*/XRT archive[5]. The source and background XRT spectra were extracted with xselect and standard procedures (Romano et al. 2006) were adopted to correct for the pile-up of X-ray photons. We generated the corresponding ancillary response files by the xrtmkarf task. The energy channels of XRT below 0.5 keV and above 10 keV were excluded. To include the XRT spectra to the joint broad-band spectral modelling, we grouped the energy channels by the *grppha* tool to have at least 20 counts per bin.

2.4. Spectral analysis

Throughout the paper we refer to the GBM trigger time. The LAT data were extracted and analysed for all the five time intervals defined in Fig. 1. We used gtburst performing an unbinned likelihood analysis and assuming a power-law model for the source photon spectrum[6]. We included the P8R3_TRANSIENT020E_2 instrument response function, a Galactic model template, and an isotropic template for particle background to take into account the background emission from the Milky Way, extra-galactic diffuse gamma-rays, unresolved extragalactic sources, residual (misclassified) cosmic-ray emission, and other extragalactic sources[7].

For the other instruments we used XSPEC (v12.10.0c) to perform a joint spectral analysis which combined any of the data sets of BAT, XRT, GBM, or LLE in all the time intervals. In order to account for inter-calibration uncertainties between the different instruments, we introduced multiplicative factors in the fitting models. We left these factors free to vary except for the detector with the highest count rates, i.e. NaI#6, whose factor has been frozen to 1.

The first three time intervals are fitted with a physical model for the synchrotron emission from relativistic electrons. We considered relativistic electrons injected with an energy distribution $\mathrm{d}N(\gamma)/\mathrm{d}\gamma \propto \gamma^{-p}$ between $\gamma_{\rm min}$ and $\gamma_{\rm max}$ and solved the continuity equation accounting for synchrotron losses. The spectral shape at any time t is determined by the ratio of $\gamma_{\rm min}$ to the electron cooling energy $\gamma_{\rm c}$, and by the value of p. In addition to the spectral shape, the model spectrum is specified by two other parameters that determine the energy $E_{\rm m}$ of the photons emitted by electrons of energy $\gamma_{\rm min}$ and the normalisation $F_{\rm m}$ of the $F(E)$ spectrum evaluated at $E_{\rm m}$, respectively. Such a model is not present in the XSPEC library and this approach towards parametrising the model is appropriate for the implementation in XSPEC. Therefore we built table model spectra for different combination of the free parameters and implemented these in XSPEC.

From the value of $E_{\rm m}$ and the ratio $\gamma_{\rm min}/\gamma_{\rm c}$ we can also derive the cooling energy $E_{\rm c}$ of the photons emitted by the electrons cooled down to $\gamma_{\rm c}$ using the relation $E_{\rm c} = E_{\rm m}\,(\gamma_{\rm c}/\gamma_{\rm min})^2$. So the four free parameters can be redefined to be $E_{\rm c}$, $E_{\rm m}$, p, and the normalisation $F_{\rm m}$.

Confidence ranges on these parameters were then derived within XSPEC, through the built-in Markov chain Monte Carlo algorithm (chain command). The results of the spectral analysis of all the data used in this work are reported in Table 1.

[5] http://www.swift.ac.uk/archive/

[6] https://fermi.gsfc.nasa.gov/ssc/data/analysis/scitools/gtburst.html

[7] https://fermi.gsfc.nasa.gov/ssc/data/analysis/documentation/Cicerone/Cicerone.pdf

The four free parameters defined above are also associated with the five physical quantities describing the emitting region, namely the co-moving magnetic field B', the total number of emitting electrons $N_{\rm e}$, the bulk Lorentz factor Γ, and the values of $\gamma_{\rm c}$ and $\gamma_{\rm min}$. We derive the value of the bulk Lorentz factor Γ from the onset of the afterglow (see Sect. 4). The other four physical quantities can be constrained using this value of Γ and the results of the spectral fitting (Sect. 5).

3. Results

3.1. Light curves

Figure 2 shows the light curves (counts s^{-1}) of GRB 180720B detected by three different instruments sensitive to increasing photon energies from top to bottom: NaI (8–900 keV), BGO (0.3–40 MeV), and LLE (30–100 MeV). These light curves show a main event lasting ∼35 s with numerous overlapping pulses and a very bright peak at $t \simeq 15$ s, followed by another peak at $t \simeq 50$ s. The pulses show the typical fast rise exponential decay (FRED) shape. In principle, a possible signature of the transition between the prompt and the afterglow could be a change in the variability of the light curve of the LLE data. However, given the low statistics of the LLE data from 35 s onwards, it is difficult to evaluate quantitatively the variability when the afterglow starts to dominate. Figure 3 shows the light curve (top panel) and the photon index evolution (bottom panel) obtained from the analysis of the LAT data in the energy range 100 MeV–100 GeV. The colour-coded symbols correspond to the five time intervals defined in Fig. 1, while the grey points show the results of the analysis of the LAT data on a finer temporal binning using equally spaced logarithmic temporal bins, except for the first and last time bins, which are longer to have higher photon statistics. The delay between the first photon detected by LAT in the 100 MeV–100 GeV range and the GBM trigger is approximately 5 s.

To fit the LAT spectrum in each time interval we use a power-law model. The results are resumed in Table 1. The bottom panel of Fig. 3 shows the evolution of the power-law photon spectral index. The spectrum of the emission detected by LAT up to 35 s is characterised by a soft spectrum with spectral index $\Gamma_{\rm PL} < -3$. From 35 s onwards, the LAT photon index sets on the constant value ∼−2. This spectral change is confirmed also by a finer time-resolved analysis. The softer spectrum $\Gamma_{\rm PL} \sim -4$ of the first time interval suggests that up to ∼35 s the emission detected by LAT is the spectral tail of the prompt emission spectrum extending into the LAT energy range. On the other hand, the harder spectral slope ∼−2 of the long-lived LAT emission after 35 s is a common feature of LAT GRBs (Ajello et al. 2019; Nava 2018) and we interpret this as the emission produced by the external forward shock. As shown in Fig. 3, the spectral index of ∼−2 remains constant until 900 s, i.e. long after the prompt emission has ceased. This can be an indication that in the LAT data we are observing the transition from the prompt to the afterglow emission phases.

The LAT light curve (top panel of Fig. 3) is derived by integrating the spectrum over the energy range 100 MeV–100 GeV in each temporal bin. The light curve peaks at $t_{\rm peak} \sim 78$ s (observed frame): we interpret this as the onset time of the afterglow emission and infer the bulk Lorentz factor of the outflow in Sect. 4.

From the spectral analysis we can infer that the LAT light curve, in the 0–35 s time interval, is possibly the superposition of a dominant prompt emission soft tail and a rising harder afterglow components. To characterise the time profile of only the afterglow component, we thus consider the light curve beyond 35 s (i.e. excluding the first two grey data points in Fig. 3) and

Table 1. Best-fit parameters for each different model used in the five SEDs reported in Fig. 4 of GRB 180720B.

Time interval	Data	Model	Flux [10^{-7} erg s^{-1} cm^{2}]	E_c [keV]	E_m [keV]	$p(\beta)$	Γ_{PL}	χ^2_{red}(d.o.f.)
0–35 s	GBM [10 keV–40 MeV]	Sync	142^{+7}_{-2}	75^{+5}_{-2}	2380^{+24}_{-524}	$> 3.95(< -2.98)$ @ 3σ	–	1.56 (293)
	LLE [30–100 MeV]	PL	$1.73^{+0.17}_{-0.24}$	–	–	–	$-3.44^{+0.36}_{-0.29}$	0.39 (11)
	GBM+LLE [10 keV–100 MeV]	Sync	142^{+3}_{-1}	79^{+2}_{-3}	1898^{+314}_{-58}	$4.77^{+0.49}_{-0.15}$ ($-3.39^{+0.08}_{-0.25}$)	–	1.52 (305)
	LAT [100 MeV–100 GeV]	PL	$0.34^{+0.10}_{-0.10}$	–	–	–	$-3.87^{+0.71}_{-0.71}$	–
35–70 s	GBM+LLE [10 keV–100 MeV]	Sync	$13.0^{+0.04}_{-2.2}$	25^{+83}_{-2}	519^{+57}_{-417}	$3.26^{+0.19}_{-0.64}$ ($-2.63^{+0.32}_{-0.1}$)	–	0.97(286)
	LAT [100 MeV–100 GeV]	PL	$1.41^{+0.49}_{-0.49}$	–	–	–	$-2.3^{+0.21}_{-0.21}$	–
70–120 s	XRT+BAT+GBM+LLE [0.5 keV–100 MeV]	Sync	$7.26^{+0.21}_{-0.8}$	–	$43.55^{+10.48}_{-7.9}$	$2.08^{+0.19}_{-0.04}$ ($-2.04^{+0.1}_{-0.02}$)	–	0.91 (465)
	LAT [100 MeV–100 GeV]	PL	$1.64^{+0.56}_{-0.56}$	–	–	–	$-2.17^{+0.17}_{-0.17}$	–
120–200 s	XRT+BAT+GBM [0.5 keV–40 MeV]	PL	$1.38^{+0.20}_{-0.15}$	–	–	–	-1.91 ± 0.05	0.86 (490)
	LAT [100 MeV–100 GeV]	PL	$0.96^{+0.34}_{-0.34}$	–	–	–	$-2.06^{+0.16}_{-0.16}$	–
200–500 s	XRT+BAT [0.5–150 keV]	PL	0.06 ± 0.01	–	–	–	-1.86 ± 0.03	1.03 (276)
	LAT [100 MeV–100 GeV]	PL	$0.21^{+0.08}_{-0.08}$	–	–	–	$-2.08^{+0.17}_{-0.17}$	–

Notes. The first column reports the time interval over which the spectrum has been integrated, the second column the detector whose data have been used to build the SED along with the energy range, and the third column represents the different models used to fit that data. From the fourth column onwards: energy flux computed in the energy range reported in the second column, photon energy corresponding to the electron cooling Lorentz factor E_c, photon energy corresponding to the electron injection Lorentz factor E_m, electron energy distribution slope p (corresponding high-energy photon index $\beta = -p/2 - 1$ in parentheses), power-law photon index of the LLE/LAT data, and the reduced χ^2 of the fit with the degrees of freedom in parentheses.

we fit with a smooth-joint double power law (see e.g. Ghirlanda et al. 2010) as follows:

$$R(t) = \frac{A(t/t_b)^{\alpha}}{1 + (t/t_b)^{\alpha+\beta}}, \quad (1)$$

where the free parameters are the rise and decay slopes α and β respectively, characteristic time t_b, and normalisation factor A. The best-fit parameters are $A = (3.8 \pm 0.4) \times 10^{-7}$ erg s^{-1} cm^{-2}, $\alpha = 2.4 \pm 0.7$, $\beta = 2.2 \pm 0.2$, and $t_b = 76.5 \pm 8.0$ s. The peak of the light curve is given by $t_{peak} = t_b(\alpha/\beta)^{1/(\alpha+\beta)} = 78 \pm 8$ s. This fit is shown by the dashed line in the top panel of Fig. 3.

The LAT flux rises consistently with $\sim t^2$, that is the expected behaviour in case of synchrotron emission (in the fast cooling regime) from the external shock prior to the deceleration radius in a constant ambient medium (e.g. Sari & Piran 1999). The flux decay follows a $\sim t^{-2}$ trend, which is somewhat unusual[8] but consistent with that derived by Ajello et al. (2019) (-1.88 ± 0.15).

After 78 s, the LAT flux is a significant fraction of the total emission and characterised by a nearly flat spectrum in $EF(E)$. This implies that at this time the LAT flux can be considered a proxy of the bolometric flux. Ghisellini et al. (2010) and Ackermann et al. (2013) studied the theoretical temporal evolution of the observed bolometric flux emitted by a fireball expanding in a homogeneous interstellar medium. These authors found that the flux decays as $\sim t^{-1}$ in the adiabatic regime and as $\sim t^{-10/7}$ in the radiative regime. The decay slope we find is steeper than both these theoretical predictions.

This unusual behaviour has been investigated by Panaitescu (2017), who found that the LAT light curves of bright bursts (with $>10^{-4}$ ph s^{-1}) tend to show a steeper temporal decay at early stages.

3.2. Spectral evolution

Figure 4 shows the evolution of the SED up to 500 s. This plot shows the SED obtained from the combined analysis of the XRT, GBM, and LAT/LLE data when available (first three SED) together with the independent analysis of the LAT data (for all the five time intervals). Since the photon with the highest energy detected by LAT is ∼5 GeV, we represent the LAT SEDs limited over the 0.1–10 GeV energy range.

The shaded regions corresponding to each SED show the 68% confidence interval on the model fits. These are obtained by combining the errors on the best-fit parameters and accounting for their covariance through a Monte Carlo sampling of the parameter space. In the following sections, we describe the evolution of the SEDs of GRB 180720B.

3.2.1. SED I (0–35 s): Evidence of synchrotron prompt spectrum

The first SED, corresponding to the time interval 0–35 s, is represented in red in Fig. 4 and shows a spectrum which extends

[8] Ackermann et al. (2013) and Ajello et al. (2019) reported an average temporal decay index around −1 for LAT GRB light curves.

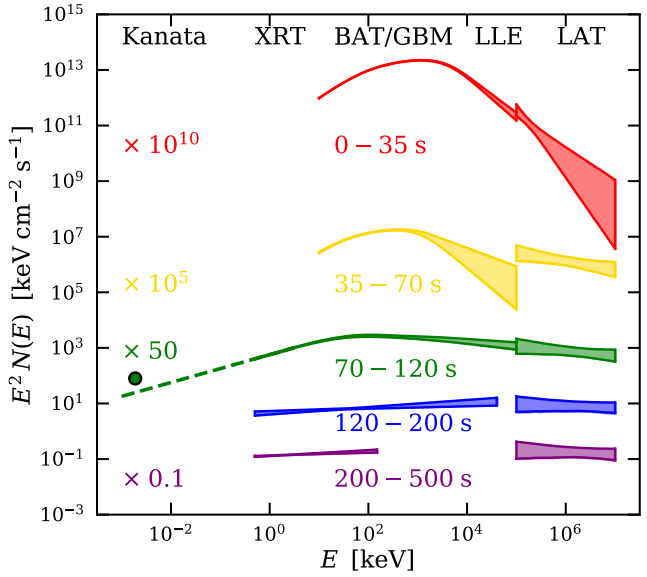

Fig. 4. Evolution of the SED of GRB 180720B. Each curve corresponds to a specific time interval and has been rescaled for presentation purposes by the scaling factor reported in the figure. For reference, the top labels denote the instruments providing data in the corresponding energy ranges.

from 10 keV all through the LAT energy range with a single emission component. The independent analysis of the LAT data (as discussed above) with a power law results in a soft emission component with slope $\Gamma_{\rm PL} = -3.87 \pm 0.71$. A similar spectral slope value is obtained from the analysis of the LLE data in the 30–100 MeV range. These spectral results are reported in Table 1.

We fitted the GBM (NaI+BGO) and LLE data together with the synchrotron model we implemented in XSPEC. The spectral parameters are reported in Table 1. The best-fit model is shown in Fig. 5 by the solid black line and the shaded yellow region represents the 68% confidence interval. The corner plot of the posterior distributions of the parameters of the fit is shown in Fig. 6, where no strong residual correlation between the free parameters is evident. The best fit, corresponding to the lowest χ^2, lies in the region characterised by the larger probability. We note that the posterior values of p correspond to $\beta = -3.39^{+0.08}_{-0.25}$, which is consistent with the value obtained by the fit of a power law to the LLE data alone (i.e. $\Gamma_{\rm PL} = -3.44^{+0.36}_{-0.29}$). The residuals of the fit (bottom panel of Fig. 5) show that the model properly fits the data over almost the entire spectral range. Systematic residuals are present below ∼30 keV over a narrow energy range. The nature of such residuals could be due to poorly calibrated response and/or to the break evolution within the considered time bin (Ravasio et al. 2019a).

The energy spectrum ($F(E) = EN(E)$) shows a slope $F(E) \propto E^{1/3}$ before the energy break $E_{\rm b} \sim E_{\rm c}$ and a slope $F(E) \propto E^{-1/2}$ between the break and the peak energy $E_{\rm p} \sim E_{\rm m}$. These results, similar to those recently found in other GRBs detected by *Swift* and *Fermi* with either empirical (e.g. Zheng et al. 2012; Oganesyan et al. 2017, 2018; Ravasio et al. 2018, 2019a) or physically motivated synchrotron models (Zhang et al. 2016; Burgess et al. 2020; Oganesyan et al. 2019), suggest that the emission is in the fast cooling regime (Kumar & McMahon 2008; Daigne et al. 2011; Beniamini & Piran 2013), even if the cooling is not complete.

The best-fit model returns a steep slope $p \sim 4.8$ of the injected electron distribution. In empirical models (e.g. Band model) this corresponds to a spectral photon index $\beta = -p/2 - 1 \sim -3.4$, which is consistent with the value obtained from the independent fit of the LLE data alone. The implication of the relatively steep p value found is discussed in Sect. 5.

As already mentioned, SED I includes the main event of this GRB, which is characterised by several overlapping pulses. A spectral analysis over such a large temporal interval could be affected by spectral evolution, with the result of producing a time averaged spectrum with a broader shape around the energy break and the energy peak. In order to explore this issue and find out if this could alter our results we performed a spectral analysis on a finer temporal resolution, by subdividing the first time interval in three bins. These time bins were chosen to have enough signal in the LLE energy range to be able to constrain the high-energy part of the spectra. The best-fit parameters for the synchrotron model are shown in Table 2. We note that the spectral break and peak tend to evolve towards lower energies as also found in Ravasio et al. (2019a). This introduces a broadening of the spectral shape as suspected. The high-energy part of the spectra is still characterised by a very steep slope, which translates into a very steep energy distribution of the electrons, as also found in the spectrum integrated over 35 s. This differs from the results of Ravasio et al. (2019a), presumably because they do not consider the LLE data.

3.2.2. SED II (35–70 s): Transition between prompt and afterglow emission

The second SED, represented in yellow in Fig. 4, shows the presence of two emission components. The spectrum below 100 MeV (obtained combining GBM and LLE data up to 100 MeV) is still fitted by the synchrotron model albeit with a harder slope of the electron energy distribution $p \sim 3.4$. The values of the peak and break energies are a factor ∼2 smaller than those of SED I. The LAT data show a harder spectrum than in the previous SED ($\Gamma_{\rm PL} = -2.3 \pm 0.2$). We note that in the following time intervals the photon index of the LAT spectrum is even harder, settling around $\Gamma_{\rm PL} \sim -2$ (as reported in Fig. 3). This suggests that we are observing the rise of the afterglow emission component at VHEs, which is characterised by a typical photon index $\Gamma_{\rm PL} \sim -2$. The superposition of this harder emission component with the peaked prompt emission spectrum as seen by the GBM can account for the harder p value obtained from the fit of the GBM+LLE data with the synchrotron model.

In conclusion, the SED in the time interval 35–70 s shows the coexistence of two different components. The prompt synchrotron emission dominates in the GBM+LLE energy range and above 100 MeV the LAT spectrum flux is inconsistent with the low-energy spectrum flux and this could indicate that the afterglow component is rising and contributing at higher energies.

3.2.3. SED III, IV, V: Evidence of afterglow emission

The time interval of the green SED from 70 s to 120 s contains the peak of the LAT light curve ($t_{\rm peak} \sim 78$ s, Fig. 3) and represents the moment when the afterglow begins to dominate the observed emission. This fact is also supported by the weak signal in the BAT and GBM energy range and by the absence of bumps in the GBM light curves (see Fig. 2). At this epoch, X-ray data from *Swift*/XRT ranging from 0.5 keV to 10 keV are also available, allowing us to extend the analysis to lower energies. We used the synchrotron model to fit the combined data of XRT+BAT+GBM+LLE. The best fit is a synchrotron

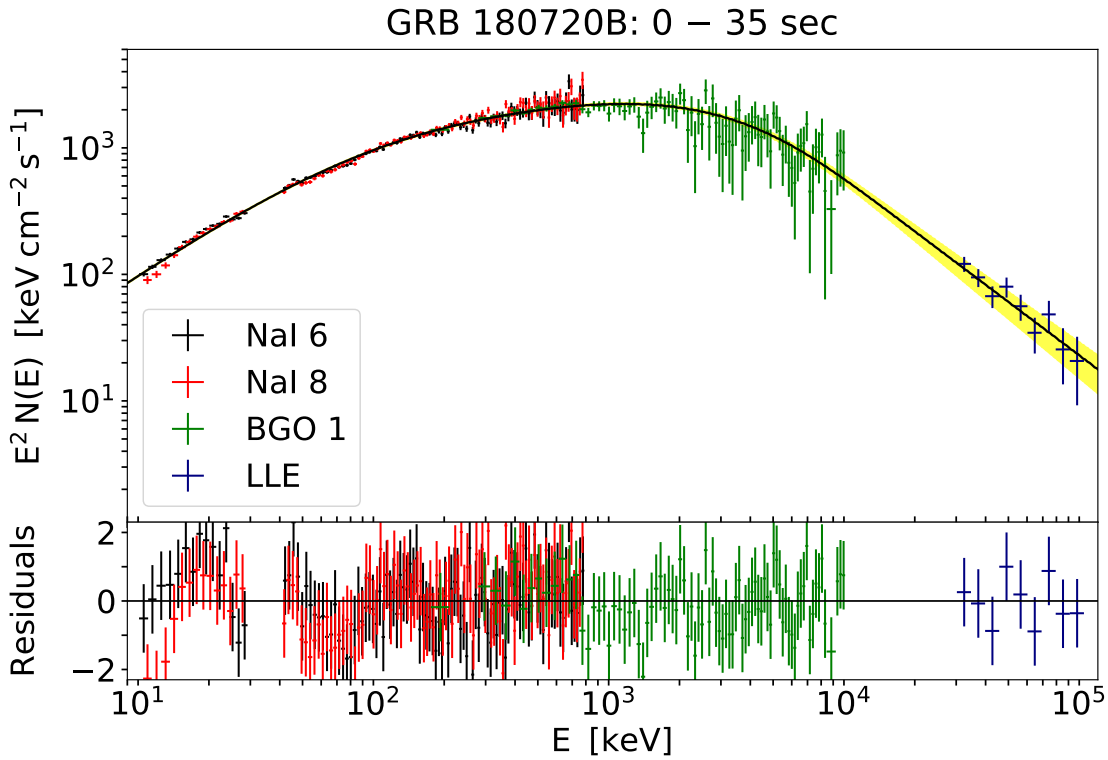

Fig. 5. Spectrum corresponding to the 0–35 s time interval. The GBM and LLE data are fitted jointly with the model (shown by the solid line) of synchrotron emission from relativistic electrons. The shaded yellow region represents the 68% confidence region of the best-fit model. *Bottom panel*: data-to-model residuals. The best-fit spectral parameters are reported in Table 1.

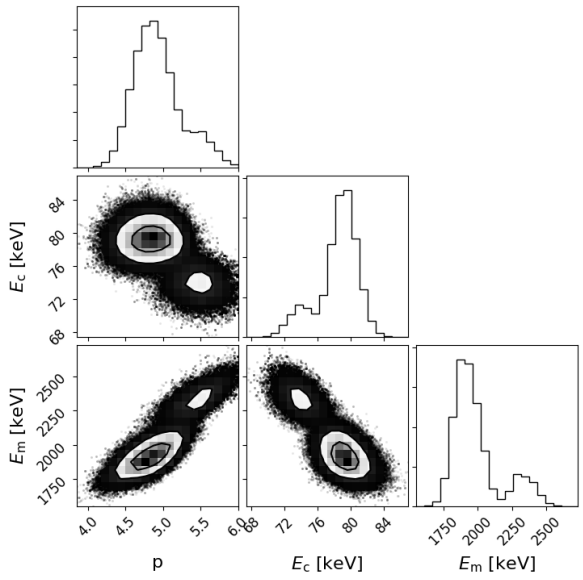

Fig. 6. Posterior distribution corner plot for the free parameters of the synchrotron model used to fit SED I. The 1D marginalised posterior distributions are shown on the diagonal, while the 2D marginalised distributions are shown below the diagonal. Contours in the 2D plots are at 1 and 2σ. Outside the 2σ contour, individual samples from our MCMC are shown as black dots.

spectrum in fast cooling, with E_c constrained to be below 0.5 keV, $E_m \sim 44$ keV and a high-energy slope which is consistent with the LAT spectrum (see also Table 1). The spectrum shows no evidence of a break down to the XRT energy range. Therefore, under the assumption that the emission is still in the fast cooling regime, at this epoch we expect that the cooling energy E_c is very low, less than 0.5 keV. Furthermore, if we extrapolate the spectrum down to the optical range with a power law $N(E) \propto E^{-3/2}$ (dashed green line in Fig. 4), it is marginally consistent with the optical detection reported by Sasada et al. 2018.

In the remaining two SEDs from 120 s up to 500 s the afterglow emission is dominant. Indeed data from X-rays up to gigelectronvolt are well fitted by a single power-law function with $\Gamma_{PL} \sim -2$, which is the expected value of the synchrotron afterglow spectral photon index (Burrows et al. 2005; Zhang et al. 2006).

4. Estimate of the bulk Lorentz factor Γ_0

The light curve of the LAT flux (Fig. 3 top panel) shows a peak at ~80 s from the trigger. After 35–40 s, the prompt emission is already too weak to contribute substantially to the observed emission in the LAT energy range. Indeed, the spectral slope of the LAT emission changes from soft to hard (Fig. 3 bottom panel).

If the long-lasting LAT emission is synchrotron radiation from the external shock, we can derive the bulk Lorentz factor just prior the deceleration phase, conventionally Γ_0, from the interpretation of the peak of the LAT light curves as the deceleration time. The different derivation of Γ_0 proposed in the literature have been summarised and compared recently in Ghirlanda et al. (2018), where it has been shown that the different methods differ at most by a factor of 2. We therefore chose the following equation derived by Nava et al. (2013):

$$\Gamma_0 = \left[\frac{(17-4s)(9-2s)3^{2-s}}{2^{10-2s}\pi(4-s)}\left(\frac{E_0}{n_0 m_p c^{5-s}}\right)\right]^{1/(8-2s)} t_{p,z}^{-\frac{3-s}{8-2s}}. \quad (2)$$

Table 2. Best-fit parameters for the synchrotron model obtained in the three time intervals in which the first SED has been split.

Time interval	Flux [10^{-7} erg s^{-1} cm^2]	E_c [keV]	E_m [keV]	$p(\beta)$	χ^2_{red}(d.o.f.)
0–14 s	170^{+4}_{-4}	156^{+5}_{-10}	2278^{+418}_{-37}	$4.98^{+0.85}_{-0.002}(-3.49^{+0.001}_{-0.43})$	1.11(341)
14–21 s	228^{+6}_{-1}	99^{+4}_{-3}	1283^{+85}_{-92}	$3.97^{+0.07}_{-0.18}(-2.99^{+0.09}_{-0.04})$	1.17(341)
27–35 s	47^{+1}_{-4}	41^{+1}_{-5}	913^{+195}_{-76}	$5.06^{+0.64}_{-0.54}(-3.53^{+0.27}_{-0.32})$	1.12(341)

Notes. For these time intervals, we used GBM and LLE data together, modelling the spectrum from 10 keV up to 100 MeV. The first column reports the time interval over which the spectrum has been integrated. The second column onwards list the following fit parameters: energy flux computed in the energy range 10 keV–100 MeV, photon energy E_c corresponding to the electron cooling Lorentz factor γ_c, photon energy $E_m$corresponding to the electron injection Lorentz factor γ_m, electron energy distribution slope p (corresponding high-energy photon index $\beta = -p/2-1$ in parentheses), and the reduced χ^2 of the fit with the degrees of freedom in parentheses.

In this equation, $t_{p,z}$ is the rest-frame onset time, i.e. $t_{p,z} = t_p/(1+z)$ and m_p is the proton mass. The kinetic energy of the fireball is inferred as $E_0 = E_{iso}(1-\eta)/\eta$, i.e. the leftovers of the prompt emission, where η is the efficiency of conversion of the initial energy into radiation during the prompt phase, typically assumed to be of few tens percent. The radial density profile is parametrised as $n = n_0 R^{-s}$, where R is the distance from the central engine. We consider the uniform density ($s = 0$) case and the scenario of a stellar wind density profile ($s = 2$). In the wind case $n_0 = \dot{M}_w/(4\pi v_w m_p)$, where $\dot{M}_w$ is the rate of mass loss and v_w is the wind speed.

Assuming a redshift $z = 0.654$ as reported in Vreeswijk et al. (2018), an isotropic equivalent energy $E_{iso} = 6\times10^{53}$ erg (Frederiks et al. 2018), $\eta = 0.2$, $t_p = 80$ s, we estimate $\Gamma_0 = 294(220)$ for $n_0 = 1\ (10)\,\mathrm{cm^{-3}}$ in the case of a constant external medium density ($s = 0$ in Eq. (2)). For a wind medium ($s = 2$ in Eq. (2)), assuming a wind mass–loss rate $\dot{M}_w = 10^{-5}\ M_\odot\ \mathrm{yr^{-1}}$, we obtain $\Gamma_0 = 142(80)$ for $v_w = 10^3\ (10^2)\,\mathrm{km\,s^{-1}}$. Such values are consistent with the distributions of Γ_0 in both scenarios obtained from the analysis of a large sample of bursts with measured onset time (Ghirlanda et al. 2018).

5. Discussion

5.1. Prompt emission

The synchrotron model presented in this work provides an acceptable fit of the prompt emission spectra of GRB 180720B in the energy range between 10 keV and 100 MeV. Under the assumption of one-shot electron acceleration, we can derive the physical parameters of the emission region in the co-moving frame of the outflow, i.e. the magnetic field B', the minimum energy of the injected non–thermal distribution of relativistic electrons γ_{min} and the total number of electrons N_e contributing to the observed emission, from the spectral properties obtained from the fit, in particular the cooling energy E_c, injection energy E_m, and flux density at the cooling energy F_c.

Following Kumar & McMahon (2008) (see also Beniamini & Piran 2013) we used the following set of equations from Oganesyan et al. (2019):

$$E_c = h\nu_c = \frac{27\pi\, e\, h\, m_e\, c\,(1+z)}{\sigma_T^2\, B'^3\, t_c^2\, \Gamma} \tag{3}$$

$$E_m = h\nu_m = \frac{3\, e\, h\, B'\, \gamma_{min}^2\, \Gamma}{4\pi\, m_e\, c\,(1+z)} \tag{4}$$

$$F_c = \frac{\sqrt{3}\, e^3\, B'\, N_e\, \Gamma\,(1+z)}{4\pi d_L^2\, m_e\, c^2}, \tag{5}$$

where d_L is the luminosity distance of the GRB, t_c is the observer-frame cooling time, Γ is the bulk Lorentz factor, and F_c is the flux at E_c. The cooling time is defined as the timescale for which the electrons lose half of their energy ($t_{c'} = \gamma/\dot{\gamma}$, in the co-moving frame). Considering only synchrotron cooling, we can find the unknowns B', γ_{min}, and N_e in terms of the observables,

$$B' = \left(\frac{27\pi\, e\, h\, m_e\, c\,(1+z)}{\sigma_T^2\, E_c\, t_c^2\, \Gamma}\right)^{1/3} \simeq 10\, E_{c,2}^{-1/3}\, t_c^{-2/3}\, \Gamma_2^{-1/3}\,(1+z)^{1/3}\ \mathrm{G} \tag{6}$$

$$\gamma_{min} = \left(\frac{4\pi\, m_e\, c\, E_m\,(1+z)}{3\, h\, e\, B'\, \Gamma}\right)^{1/2} \simeq 6.3\times10^5\, E_{m,3}^{1/2}\, B'^{-1/2}\, \Gamma_2^{-1/2}\,(1+z)^{1/2} \tag{7}$$

$$N_e = \frac{4\pi d_L^2\, m_e\, c^2\, F_c}{\sqrt{3}\, e^3\, B'\, \Gamma\,(1+z)} \simeq 10^{50}\, F_{c,mJy}\, B'^{-1}\, \Gamma_2^{-1}\, d_{L,28}^2\,(1+z)^{-1}, \tag{8}$$

where E_c is expressed in units of 10^2 keV, E_m in units of 10^3 keV, Γ in units of 100, and F_c in mJy and d_L in units of 10^{28} cm. The fit of the spectrum corresponding to SED I (see Fig. 5) returns a cooling energy $E_c \sim 79$ keV and an injection energy $E_m \sim 1898$ keV. We also derive the flux at the cooling energy $F_c \sim 6$ mJy. The integration time of 35 s of SED I corresponds to the time (in the observer frame) needed by the injected electrons to cool down to γ_c. The emission of these electrons produces a spectral break at an observed energy similar to the cooling energy $\sim E_c$. We remark that the relative positions of the cooling energy E_c and of the injection energy E_m in SED I lead to a value of the Lorentz factor γ_c of the cooled electrons, which is only a factor of 5 lower than the injection Lorentz factor γ_{min}. This indicates that the electrons are in a moderately fast cooling regime. Therefore, in Eq. (5) we use $E_c = 79$ keV and $t_c = 35$ s. Considering the maximum range of possible values of Γ, i.e. 294 (80) in the homogeneous (wind) medium case, we find $B' \sim 0.8\ (1.3)$ G, $\gamma_{min} \sim 0.9\ (1.3)\times10^6$ and $N_e \sim 1.2\ (2.9)\times10^{51}$. The uncertainties on the measured quantities E_c, E_m, F_c give an uncertainty of 20% on the physical parameters. Also the values of B', γ_{min}, and N_e inferred from a finer time resolved analysis are consistent with the values inferred from the spectrum integrated over the first 35 s. This is an indication that the physical properties of the outflow do not change significantly during the prompt emission. These values are also consistent with the ranges estimated by Oganesyan et al. (2019) for a sample of 21 *Swift* GRBs.

As found above, the low-energy break in the spectrum, identified as a radiative cooling break, inevitably implies a low value

of the magnetic field. The emitting region, on the other hand, should lie at a large distance from the central power house, as indicated by the derived large bulk Lorentz factor and by assuming that the cooling timescale is of the same order of the dynamical time. This in turn implies a reduced radiation energy density and therefore a reduced SSC luminosity. Furthermore the large values of γ_m and γ_c ensure that the self-Compton emission occurs in the Klein–Nishina regime further limiting the SSC component (Oganesyan et al. 2019) and most of it would be produced at very large frequencies. More quantitatively, with a magnetic field of 1 G, $\Gamma = 300$ and $t_c \sim 35$ s we can infer a distance of $R \sim 10^{17}$ cm. This implies that the SSC luminosity would exceed the synchrotron one by a factor 100 if the scatterings occur in the Thomson regime. Taking into account the reduction by a factor 10^4 because of the Klein–Nishina regime (Ghisellini et al. 2020), eventually the bolometric SSC prompt luminosity is expected to be a factor of 100 lower than the synchrotron luminosity, and most of it would be produced at around 100 TeV, well above the *Fermi*/LAT energy range. Therefore the SSC contribution in the LAT energy range and below could be safely neglected. However the Klein–Nishina regime could also modify the spectral shape of the synchrotron spectrum at lower energies. Following the work by Daigne et al. (2011) we verified that for the estimated values of B', γ_{min}, γ_c, N_e, and Γ_0, the Klein–Nishina regime does not lead to significant deviations from a pure synchrotron spectrum as assumed in performing the analysis.

The best-fit value from SED I for the electron spectral index is $p = 4.8$ (Fig. 5). This in turn produces a soft photon spectrum ($\beta \sim -3.4$) at high energies as confirmed by the independent fit of the high-energy spectrum with a single power law. Mildly relativistic shocks, produced for example by the dissipation of the kinetic energy of different colliding shells (internal shock scenario Rees & Meszaros 1994), can hardly produce large values of p and γ_{min}. An efficient shock, as expected in low magnetised[9] plasma (e.g. Sironi & Spitkovsky 2011; Sironi et al. 2015a), can accelerate particles to large γ_{min}, but typically converts a fraction (around 10%) of the kinetic energy into a hard ($p \sim 2-2.4$) non-thermal electron energy distribution (Heavens & Drury 1988; Rees & Meszaros 1994; Kennel & Coroniti 1984).

Magnetic reconnection (Spruit et al. 2001; Drenkhahn & Spruit 2002), as also recently shown by particle in cell simulations (Sironi & Spitkovsky 2014; Sironi et al. 2015b; Petropoulou et al. 2019), can produce a steep electron energy distributions (i.e. $p \sim 4-5$) if the burst outflow has a high pair-proton number ratio ($\kappa \sim 200$) and a moderate magnetisation parameter $\sigma \sim 1$. However, with such parameter values, the electrons can only attain a moderately large $\gamma_e \sim 10^2-10^3$. Different combinations of the leading parameters, however, could reconcile these values with those estimated in our analysis.

If we compare the first SED I (0–35 s) with the second SED II (35–70 s), we find that the value of p decreases from $p \sim 4.8$ to $p \sim 3.4$, thus corresponding to a harder electron energy distribution producing the synchrotron spectrum of SED II. However, we cannot exclude that also in SED II the value of p is uncommonly large because of the contamination of the high-energy part of the spectrum by the harder spectral component arising in the LAT energy range.

In conclusion, the acceleration mechanism responsible for the injection of non-thermal electrons must be really efficient in accelerating electrons to VHEs, but it also should give rise to a steep electron energy distribution. According to the standard theory and simulations, shocks or magnetic reconnection seem unable to easily produce injected electron distributions with such properties.

5.2. Connections between LAT and H.E.S.S. emissions

The H.E.S.S. telescope detected high-energy photons (~300 GeV) from GRB 180720B at ~10.5 h after the trigger time. Wang et al. (2019) and Abdalla et al. (2019) report a H.E.S.S. $EF(E)$ flux of 5×10^{-11} erg cm^{-2} s^{-1} in the energy range 100–440 GeV.

By analysing the LAT data from 8 to 12 hours after the trigger, we obtain[10] a 1σ upper limit of 8.5×10^{-10} erg cm^{-2} s^{-1} (integrated in the 0.1–100 GeV energy range). This value agrees with the LAT upper limit estimated by Wang et al. (2019). By extrapolating the LAT light curve of Fig. 3 at $t \sim 10.5$ h, we predict a 0.1–100 GeV $EF(E)$ flux of $\sim5 \times 10^{-13}$ erg cm^{-2} s^{-1} if the flux decays $\propto t^{-2.2}$ (as found in the first 500 s). Instead, if after ~500 s the flux temporal decay becomes shallower (e.g. $\propto t^{-1}$, consistently with the X-ray data[11]), the flux at 10.5 hours would be $\sim8 \times 10^{-11}$ erg cm^{-2} s^{-1}.

Therefore, the true LAT flux at around 10 h should be between $\sim5 \times 10^{-13}$ erg cm^{-2} s^{-1} and the upper limit 8.5×10^{-10} erg cm^{-2} s^{-1}. We note that if the flux decays $\propto t^{-1}$, its value at 10.5 h is similar to that reported by Wang et al. (2019) and Abdalla et al. (2019) for the H.E.S.S. detection at higher energies. The similarity in the $EF(E)$ flux values leads to the possible interpretation that the afterglow spectrum above 100 MeV could extend up to energies around 300 GeV as a single component. However the VHE emission is unlikely to be synchrotron emission because of the limiting maximum synchrotron frequency (Guilbert et al. 1983). This VHE emission can be more easily explained as a SSC component (Meszaros et al. 1994; Waxman 1997; Wei & Lu 1998) as also suggested by Wang et al. (2019) and Abdalla et al. (2019).

6. Summary and conclusions

In this paper we have studied both the prompt and the very early afterglow emission of GRB 180720B. The spectral evolution of the burst up to 500 s after the trigger time is shown in Fig. 4. The SED evolution (Fig. 4) shows the emergence of the afterglow component in the LAT energy range and the progressive turning off of the prompt emission (which dominates up to 70 s – SED I and II – in the 0.01–1 MeV energy range).

The LAT light curve shows a peak which we interpret as due to the deceleration of the outflow (Fig. 3). The peak time provides an estimate of the bulk Lorentz factor $\Gamma_0 \sim 300$ (150) for a homogeneous (wind-like) circum-burst medium.

The SED of the first three time intervals were fitted (through XSPEC) with a physical model of synchrotron emission from a relativistic population of injected electrons. From the SED accumulated over the first 35 s, we find that the emitting electrons should be injected with a steep power-law energy distribution with $p \sim 4.8$.

From the spectral features of the first 35 s SED, we were able to estimate the intrinsic physical parameters of the emission region during the prompt phase. In particular, the co-moving

[9] The magnetisation σ is defined as the ratio of the energy densities in magnetic field to particles, respectively, evaluated in the co-moving frame of the emission region.

[10] We assume that the spectral index of the LAT emission component is −2 as observed before.

[11] https://www.swift.ac.uk/xrt_curves/00848890/

magnetic field $B' \sim 1$ G, the minimum electron Lorentz factor $\gamma_{\rm min} \sim 10^6$, and the total number of electrons $N_{\rm e} \sim 10^{51}$. Large values of $\gamma_{\rm min}$ and p require an efficient acceleration mechanism and a "soft" energy distribution of accelerated particles, which challenge the current understanding of particle acceleration through mildly relativistic shocks or magnetic reconnection.

We also find that *Fermi*/LAT did not detect any emission at the epoch (10.5 h) of the claimed H.E.S.S. detection and derive an upper limit on the LAT flux (0.1–100 GeV), which is above the flux reported by H.E.S.S. (in the 100–440 GeV energy range). The extrapolation of the LAT light curve at 10.5 h gives a 0.1–100 GeV flux consistent with the flux level detected by H.E.S.S. A single component synchrotron spectrum extending beyond 100 GeV energies is unlikely, therefore a high-energy SSC component seems to be a viable scenario to explain the late time H.E.S.S. detection at VHE.

Acknowledgements. This research has made use of data obtained through the High Energy Astrophysics Science Archive Research Center Online Service, provided by the NASA/Goddard Space Flight Center, and specifically this work made use of public *Fermi*/GBM data and of data supplied by the UK Swift Science Data Centre at the University of Leicester. We also would like to thank for support the implementing agreement ASI-INAF n. 2017-14-H.0. We acknowledge the PRIN INAF CTA-SKA project "Towards the SKA and CTA era: discovery, localisation, and physics of transient sources" and the PRIN-MIUR project "Figaro" for financial support.

References

Abdalla, H., Adam, R., Aharonian, F., et al. 2019, Nature, 575, 464
Ackermann, M., Ajello, M., Asano, K., et al. 2013, ApJS, 209, 11
Ajello, M., Arimoto, M., Axelsson, M., et al. 2019, ApJ, 878, 52
Atwood, W. B., Abdo, A. A., Ackermann, M., et al. 2009, ApJ, 697, 1071
Barthelmy, S. D., Cummings, J. R., Krimm, H. A., et al. 2018, GRB Coordinates Network, 22998, 1
Bellm, E. C., & Cenko, S. B. 2018, GRB Coordinates Network, 23041, 1
Beniamini, P., & Piran, T. 2013, ApJ, 769, 69
Beniamini, P., Nava, L., Duran, R. B., & Piran, T. 2015, MNRAS, 454, 1073
Bissaldi, E., & Racusin, J. L. 2018, GRB Coordinates Network, 22980, 1
Burgess, J. M., Bégué, D., Bacelj, A., et al. 2020, Nat. Astron., 4, 174
Burrows, D. N., Hill, J. E., Chincarini, G., et al. 2005, ApJ, 622, L85
Chandra, P., Nayana, A. J., Bhattacharya, D., Cenko, S. B., & Corsi, A. 2018, GRB Coordinates Network, 23073, 1
Cherry, M. L., Yoshida, A., Sakamoto, T., et al. 2018, GRB Coordinates Network, 23042, 1
Covino, S., & Fugazza, D. 2018, GRB Coordinates Network, 23021, 1
Crouzet, N., & Malesani, D. B. 2018, GRB Coordinates Network, 22988, 1
Daigne, F., & Mochkovitch, R. 1998, MNRAS, 296, 275
Daigne, F., Bošnjak, Ž., & Dubus, G. 2011, A&A, 526, A110
Derishev, E., & Piran, T. 2019, ApJ, 880, L27
Drenkhahn, G., & Spruit, H. C. 2002, A&A, 391, 1141
Fraija, N., Barniol Duran, R., Dichiara, S., & Beniamini, P. 2019, ApJ, 883, 162
Frederiks, D., Golenetskii, S., Aptekar, R., et al. 2018, GRB Coordinates Network, 23011, 1
Gehrels, N., Chincarini, G., Giommi, P., et al. 2004, ApJ, 611, 1005
Ghirlanda, G., Nava, L., Ghisellini, G., Celotti, A., & Firmani, C. 2009, A&A, 496, 585
Ghirlanda, G., Ghisellini, G., & Nava, L. 2010, A&A, 510, L7
Ghirlanda, G., Nappo, F., Ghisellini, G., et al. 2018, A&A, 609, A112
Ghisellini, G., Celotti, A., & Lazzati, D. 2000, MNRAS, 313, L1
Ghisellini, G., Ghirlanda, G., Nava, L., & Celotti, A. 2010, MNRAS, 403, 926
Ghisellini, G., Ghirlanda, G., Oganesyan, G., et al. 2020, A&A, in press https://doi.org/10.1051/0004-6361/201937244
Gruber, D., Goldstein, A., Weller von Ahlefeld, V., et al. 2014, ApJS, 211, 12
Guilbert, P. W., Fabian, A. C., & Rees, M. J. 1983, MNRAS, 205, 593
Heavens, A. F., & Drury, L. O. 1988, MNRAS, 235, 997
Horiuchi, T., Hanayama, H., Honma, M., et al. 2018, GRB Coordinates Network, 23004, 1
Itoh, R., Murata, K. L., Tachibana, Y., et al. 2018, GRB Coordinates Network, 22983, 1
Izzo, L., Kann, D. A., de Ugarte Postigo, A., et al. 2018, GRB Coordinates Network, 23040, 1
Jelinek, M., Strobl, J., Hudec, R., & Polasek, C. 2018, GRB Coordinates Network, 23024, 1
Kaneko, Y., Preece, R. D., Briggs, M. S., et al. 2006, ApJS, 166, 298
Kann, D. A., Izzo, L., & Casanova, V. 2018, GRB Coordinates Network, 22985, 1
Kennel, C. F., & Coroniti, F. V. 1984, ApJ, 283, 710
Kobayashi, S., Piran, T., & Sari, R. 1997, ApJ, 490, 92
Kumar, P., & Barniol Duran, R. 2009, MNRAS, 400, L75
Kumar, P., & Barniol Duran, R. 2010, MNRAS, 409, 226
Kumar, P., & McMahon, E. 2008, MNRAS, 384, 33
Kumar, P., & Zhang, B. 2015, Phys. Rep., 561, 1
Lipunov, V., Gorbovskoy, E., Tiurina, N., et al. 2018, GRB Coordinates Network, 23023, 1
Meegan, C., Lichti, G., Bhat, P. N., et al. 2009, ApJ, 702, 791
Meszaros, P. 2019, Mem. Soc. Astron. It., 90, 57
Meszaros, P., & Rees, M. J. 1993, ApJ, 405, 278
Meszaros, P., Rees, M. J., & Papathanassiou, H. 1994, ApJ, 432, 181
Mirzoyan, R. 2019, Astron. Tel., 12390, 1
Nava, L. 2018, Int. J. Mod. Phys. D, 27, 1842003
Nava, L., Ghirlanda, G., Ghisellini, G., & Celotti, A. 2011, A&A, 530, A21
Nava, L., Sironi, L., Ghisellini, G., Celotti, A., & Ghirlanda, G. 2013, MNRAS, 433, 2107
Negoro, H., Tanimoto, A., Nakajima, M., et al. 2018, GRB Coordinates Network, 22993, 1
Oganesyan, G., Nava, L., Ghirlanda, G., & Celotti, A. 2017, ApJ, 846, 137
Oganesyan, G., Nava, L., Ghirlanda, G., & Celotti, A. 2018, A&A, 616, A138
Oganesyan, G., Nava, L., Ghirlanda, G., Melandri, A., & Celotti, A. 2019, A&A, 628, A59
Panaitescu, A. 2017, ApJ, 837, 13
Pelassa, V., Preece, R., Piron, F., et al. 2010, ArXiv e-prints [arXiv:1002.2617]
Petropoulou, M., Sironi, L., Spitkovsky, A., & Giannios, D. 2019, ApJ, 880, 37
Piran, T. 1999, Nucl. Phys. B Proc. Suppl., 70, 431
Piran, T. 2004, Rev. Mod. Phys., 76, 1143
Preece, R. D., Briggs, M. S., Mallozzi, R. S., et al. 1998, ApJ, 506, L23
Ravasio, M. E., Oganesyan, G., Ghirlanda, G., et al. 2018, A&A, 613, A16
Ravasio, M. E., Ghirlanda, G., Nava, L., & Ghisellini, G. 2019a, A&A, 625, A60
Ravasio, M. E., Oganesyan, G., Salafia, O. S., et al. 2019b, A&A, 626, A12
Rees, M. J., & Meszaros, P. 1992, MNRAS, 258, 41
Rees, M. J., & Meszaros, P. 1994, ApJ, 430, L93
Reva, I., Pozanenko, A., Volnova, A., et al. 2018, GRB Coordinates Network, 22979, 1
Roberts, O. J., & Meegan, C. 2018, GRB Coordinates Network, 22981, 1
Romano, P., Campana, S., Chincarini, G., et al. 2006, A&A, 456, 917
Ruiz-Velasco, E. L. 2019, in 1st International Cherenkov Telescope Array Symposium – Exploring the High-Energy Universe with CTA, Bologna, 6–9 May 2019
Sari, R., & Piran, T. 1997, MNRAS, 287, 110
Sari, R., & Piran, T. 1999, A&AS, 138, 537
Sasada, M., Nakaoka, T., Kawabata, M., et al. 2018, GRB Coordinates Network, 22977, 1
Schmalz, S., Graziani, F., Pozanenko, A., et al. 2018, GRB Coordinates Network, 23020, 1
Sfaradi, I., Bright, J., Horesh, A., et al. 2018, GRB Coordinates Network, 23037, 1
Siegel, M. H., Burrows, D. N., Deich, A., et al. 2018, GRB Coordinates Network, 22973, 1
Sironi, L., & Spitkovsky, A. 2011, ApJ, 726, 75
Sironi, L., & Spitkovsky, A. 2014, ApJ, 783, L21
Sironi, L., Keshet, U., & Lemoine, M. 2015a, Space Sci. Rev., 191, 519
Sironi, L., Petropoulou, M., & Giannios, D. 2015b, MNRAS, 450, 183
Spruit, H. C., Daigne, F., & Drenkhahn, G. 2001, A&A, 369, 694
Vreeswijk, P. M., Kann, D. A., Heintz, K. E., et al. 2018, GRB Coordinates Network, 22996, 1
Wang, X.-Y., Liu, R.-Y., Zhang, H.-M., Xi, S.-Q., & Zhang, B. 2019, ApJ, 884, 117
Watson, A. M., Butler, N., Becerra, R. L., et al. 2018, GRB Coordinates Network, 23017, 1
Waxman, E. 1997, ApJ, 485, L5
Wei, D. M., & Lu, T. 1998, ApJ, 505, 252
Wells, A., Burrows, D. N., Hill, J. E., et al. 2004, in Gamma-Ray Bursts: 30 Years of Discovery, eds. E. Fenimore, & M. Galassi, AIP Conf. Ser., 727, 642
Zhang, B. 2019, AAS/High Energy Astrophysics Division, 201.03
Zhang, B., Fan, Y. Z., Dyks, J., et al. 2006, ApJ, 642, 354
Zhang, B.-B., Uhm, Z. L., Connaughton, V., Briggs, M. S., & Zhang, B. 2016, ApJ, 816, 72
Zheng, W., & Filippenko, A. V. 2018, GRB Coordinates Network, 23033, 1
Zheng, W., Shen, R. F., Sakamoto, T., et al. 2012, ApJ, 751, 90